



# Mitigating laminar-turbulent transition in hypersonic flow using bio-inspired surface patterns

Wenkai Zhu, Shan Zhong, Johan Steelant

# **Abstract**

This present investigation focuses on the development and application of herringbone riblets to delay boundary layer laminar-turbulent transition in hypersonic flow. A series of wind tunnel experiments were conducted on a 270 mm long flared cone model at Mach 5 in the High-Supersonic Tunnel (HSST) at University of Manchester. Herringbone riblets, produced via laser manufacturing techniques, were evaluated for their influence on boundary layer transition, using high-speed schlieren imaging. The effects of riblet height and placement along the model were systematically examined. It was found that riblets with a height of 54  $\mu$ m placed at 170 mm from the leading edge of the model delayed the onset of transition at a unit Reynolds number of Re<sub>unit</sub> =  $10\times10^6$  m $^{-1}$ , demonstrating their potential as a means of effective flow control in hypersonic flow.

**Keywords:** hypersonic boundary layer transition, herringbone riblets

# **Nomenclature**

Latin

s -- Riblet spacingh -- Riblet height

w -Riblet width l -Riblet length

RMS -- Root-mean-square

#### Greek

- $\theta$  -- Divergent angle between the left- and right-tilted grooves
- $\alpha$  -- Half of the included angle between the two groove directions
- $\delta_p$  -- Distance between the point of maximum density gradient and the model surface
- $\Lambda$  -- Riblet spanwise wavelength

## 1. Introduction

Hypersonic boundary-layer transition plays a critical role in the design of hypersonic vehicles. During the process of transition to turbulence and its subsequent development, skin friction and aerodynamic drag increase significantly, posing major challenges for the thermal protection systems of such vehicles [1, 2, 3]. A deeper understanding of hypersonic boundary-layer transition, along with effective methods to control the evolution of disturbances within the boundary layer, can lead to savings in weight of thermal protection systems which will subsequently translate to lower costs and higher payload capability [4].

Various passive flow-control techniques have been investigated to stabilize disturbances that lead to boundary-layer transition in hypersonic flows. Studies have shown that the careful placement of two-dimensional (2D) roughness elements, such as half-ellipse strips [5] and surface waviness [6], can

<sup>&</sup>lt;sup>1</sup>Department of Mechanical and Aerospace Engineering, University of Manchester, Manchester, United Kingdom, wenkai.zhu@manchester.ac.uk

<sup>&</sup>lt;sup>2</sup>Department of Mechanical and Aerospace Engineering, University of Manchester, Manchester, United Kingdom, shan.zhong@manchester.ac.uk

<sup>&</sup>lt;sup>3</sup>European Space Research and Technology Centre, Noordwijk, The Netherlands, johan.steelant@esa.int

suppress dominant Mack-mode instabilities by altering the base flow and modifying disturbance amplification characteristics. Similarly, small three-dimensional (3D) roughness elements, such as spherical roughness and vortex generators [7, 8] have been demonstrated to generate appropriately tuned streamwise streaks that stabilize Mack-mode waves. Furthermore, porous surfaces with either regular or random structures have been found to attenuate second-mode instabilities [9, 10].

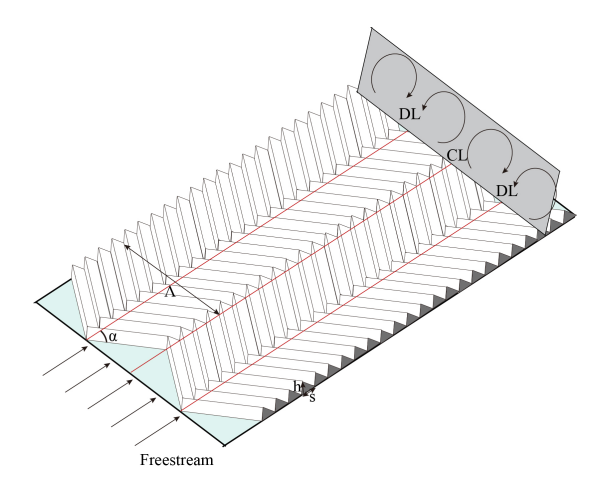


**Fig 1.** Schematic of herringbone riblets (or convergent–divergent riblets) and the secondary flow they generate in the boundary layer.

Herringbone riblets—also known as convergent—divergent (C–D) riblets—are a class of surface textures that have recently attracted increasing research interest. These structures consist of alternating left-and right-tilted microgrooves arranged side by side. Their design is inspired by the microstructures found on the secondary flight feathers of birds [11, 12, 13, 14]. Despite their microscale dimensions, these riblets are highly effective in inducing large-scale secondary flow motions (commonly referred to as roll modes) within the boundary layer. These roll modes generate an upwash along the converging lines (CL) and a downwash along the diverging lines (DL), as illustrated in figure 1.

Herringbone riblets have been demonstrated to be an effective method of flow control in various applications. Chen et al. [11] demonstrated that applying herringbone riblets to the inner surface of a circular pipe can achieve a 17% reduction in turbulent friction drag. Liu et al. [15] showed that herringbone riblets mounted on the suction surfaces of highly loaded diffuser blades can significantly reduce pressure losses and increase the flow turning angle in a linear cascade. In this case, the roll modes generated by the riblets are believed to suppress flow separation on the suction surfaces via increased mixing. Quan et al. [16] found that herringbone riblets are capable of suppressing shock-induced flow separation at Mach 5, thereby enhancing pressure recovery. Moreover, their study revealed that these microscale riblets induce large-scale roll modes within the boundary layer, similar to those observed in incompressible flows. Wen et al. [17] demonstrated that herringbone riblets can significantly modify the shockwave—boundary layer interaction zone and reduce the size of the separation bubble.

Motivated by this bio-inspired concept, the present study investigates the effect of herringbone riblets on delaying boundary-layer transition in hypersonic flow over a flared cone.

# 2. Experimental setup

#### 2.1. HSST Wind Tunnel

The experiments were undertaken in the High SuperSonic Tunnel (HSST) of the University of Manchester, as shown schematically in figure 2. This blow-down hypersonic facility generates Mach 5 airflow through an axisymmetric nozzle, featuring a 152 mm exit diameter and an open-jet test section. In our experiments, the plenum total temperature was fixed at 410 K and the freestream total pressure was

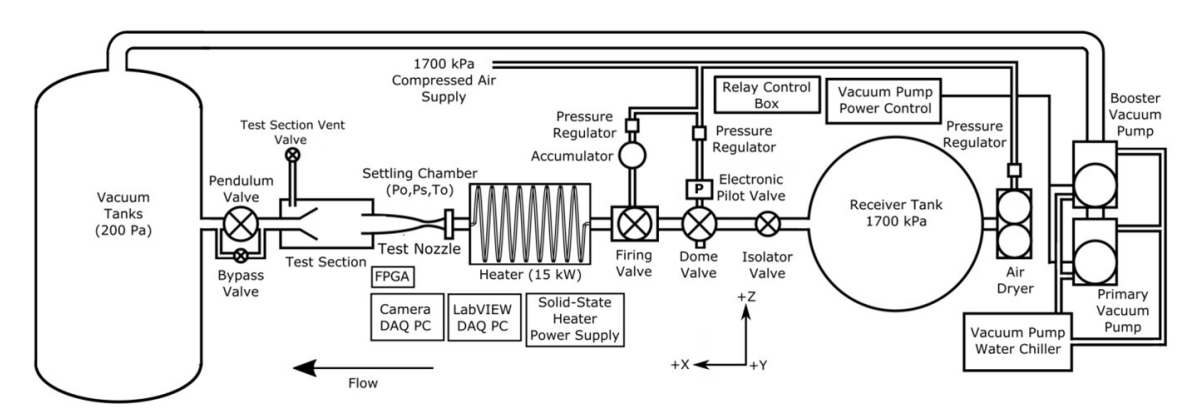


Fig 2. Schematic of the HSST configuration

varied to enable an adjustment of the Reynolds number. The tunnel allows continuous operation for up to 7.5 seconds.

#### 2.2. Flared cone model and herringbone riblets

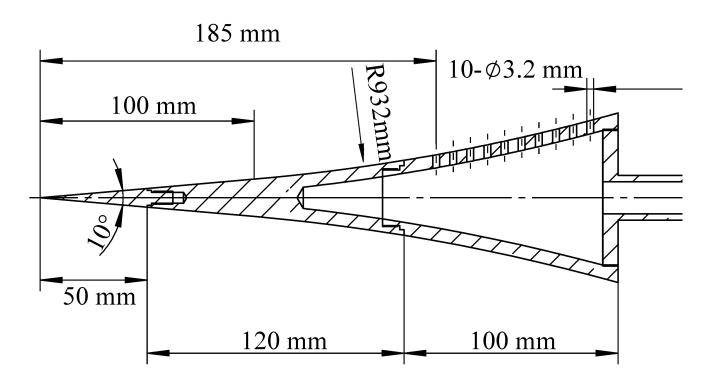


Fig 3. Schematic of the flared cone model

The model, illustrated schematically in Figure 3, is based on previous designs with minor modifications [18, 19]. It is a flared cone with an overall length of 270 mm. The geometry comprises a  $5^{\circ}$  half-angle circular cone extending over the first 100 mm, followed by a tangent flare with a radius of 932 mm, reaching the model base at 270 mm. The model is divided into three segments: the first 50 mm is made of stainless steel; the middle 120 mm is Bakelite; and the final 100 mm is a Bakelite shell. The model components are threaded together and mounted coaxially with the nozzle at zero angle of attack. The unaffected core flow extends more than 300 mm downstream, sufficient to fully encompass the model.

As the boundary layer develops downstream, its thickness generally increases along a flat plate or a sharp cone at zero angle of attack. In contrast, under the influence of an adverse pressure gradient, the boundary layer thickness along a flared cone remains nearly constant in the streamwise direction. This condition facilitates a substantial growth of the most amplified second-mode instability, whose wavelength is approximately twice the boundary-layer thickness. In the present case, the boundary-layer thickness is about 1 mm, while the corresponding second-mode wavelength is approximately 2 mm.

The herringbone riblets used in the experiments were manufactured by removing a small amount of materials from a plastic sheet using advanced laser manufacturing techniques. Figure 4(a) shows the definition of riblet geometry. Key geometric parameters include riblet spacing (s), height (h), length (l),

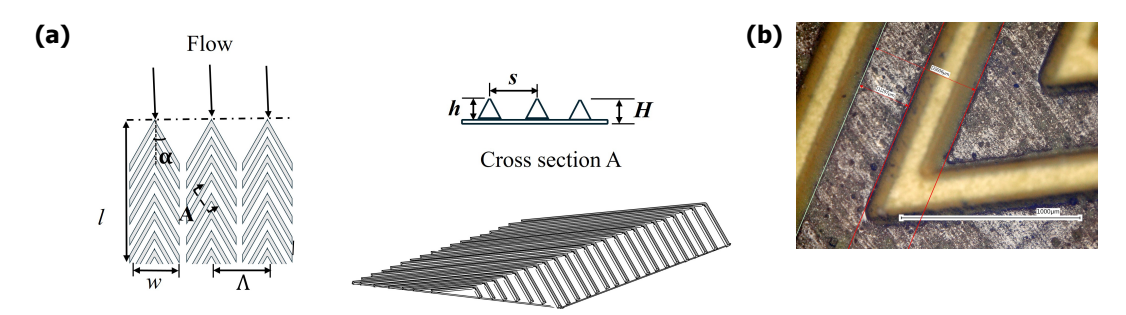
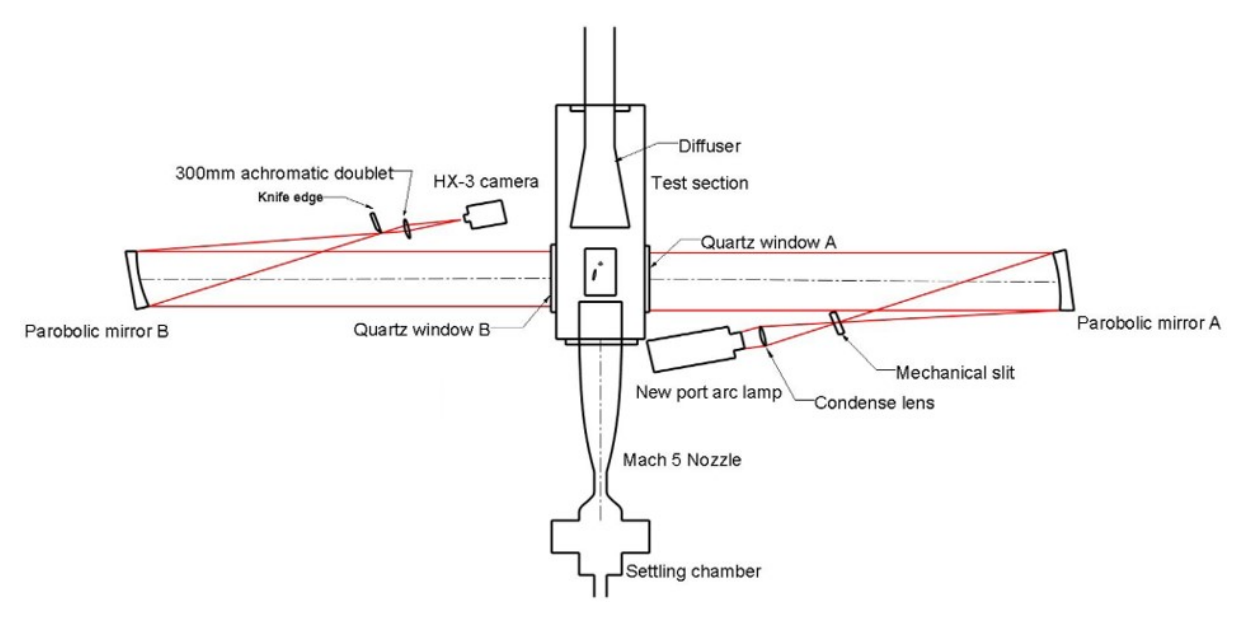


Fig 4. Design of herringbone riblets: (a) definition of riblets geometry and (b) microscopic view of the fabricated riblets.

and width (w). The divergent angle between the left- and right-tilted grooves is  $\theta$ , with the yaw angle  $\alpha = \theta/2$  measuring from each side of the centerline. The wavelength ( $\Lambda$ ) refers to the distance between the centerlines of neighboring riblets. The gap size  $(\Lambda - w)$  is defined as the empty space between two adjacent riblets. The microscopic view of the herringbone riblets is shown in Figure 4(b).

## 2.3. High-speed schlieren imaging

Toepler's Z-type Schlieren technique was adapted for flow visualization using a continuous light source (CBT-90 Green, Luminus Devices) paired with a focusing lens and a 1 mm-wide slit. The optical system incorporated two 12-inch diameter parabolic mirrors with an f/7.9 focal ratio, offering a wide and clear view of the test section. A static chip-on-board LED, with a chip area of 9 mm<sup>2</sup>, provided sufficient illumination for an ultra-high-speed camera (Phantom V1610) to capture boundary layer transition phenomena. To minimize optical aberrations such as coma and astigmatism, the parabolic mirrors were offset by 5° from their optical axes, following the approach used by Erdem et al [20].



**Fig 5.** Schematic setup of schlieren imaging system.

A collimated light beam passed through the test section windows and was focused onto a knife-edge plane oriented perpendicular to the flow direction. The focused beam was then projected onto the CMOS sensor of the camera. The sensor area was cropped to a resolution of 1024×768 pixels, yielding a spatial resolution of 6.65 pixels/mm—sufficient to resolve the key flow features. With the reduced sensor area, image acquisition was carried out at 8 kHz, enabling detailed observation of transitional

Page I 4

flow behavior. Data were temporarily stored in the camera buffer and later transferred to an external solid-state drive (SSD) for post-processing. The optical setup and data acquisition architecture are illustrated in Figure 5.

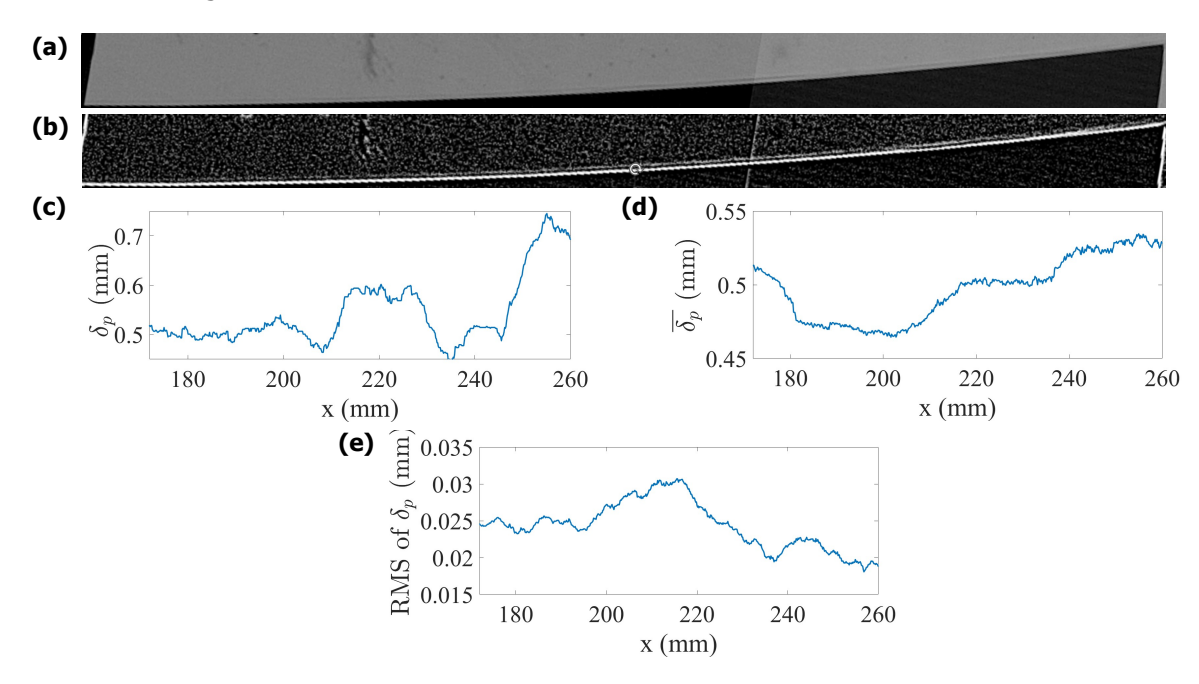


**Fig 6.** Post-processing of schlieren images: (a) raw schlieren image; (b) filtered image; (c) instantaneous positions of the maximum density gradient along the flow direction; (d) time-averaged position distribution; (e) RMS variation of the maximum density gradient positions in the streamwise direction.

Within the boundary layer, the flow velocity gradually increases from zero at the wall to the freestream velocity, resulting in a slight gradient in fluid density. This gradient leads to variations in the refractive index—regions of higher density exhibit higher refractive indices, while regions of lower density exhibit lower refractive indices. When parallel light is directed through the flow field, it is deflected to different extents depending on the local density variations within the boundary layer. The schlieren optical system captures these deflections, forming light and dark fringes on a screen. A typical schlieren image obtained from the experiment is shown in Figure 6(a). The boundary layer is initially stable, and its thickness remains nearly constant up to the midpoint of the flared cone model. Beyond this point, regular long-wavelength three-dimensional disturbances—characterized by wavelengths approximately 5 to 10 times the local boundary layer thickness—begin to emerge. The boundary layer then undergoes rapid temporal variations. Toward the downstream end of the model, the boundary layer breaks down and becomes fully turbulent, with no further regular disturbances observable.

By observing the video of schlieren images, we can qualitatively identify the onset of transition as the location where the boundary-layer thickness varies rapidly in time. In order to facilitate a more reliable comparison of different test cases, the following image processing procedure is applied to extract the quantitative information of the location of onset of transition. Raw images similar to that shown in Figure 6(a) were first cropped to the region over the flared cone that encompassed the boundary layer. Light-intensity gradient fields were computed from each instantaneous image. A  $5\times5$  high-pass filter was applied to enhance sharp gradients associated with the model surface and the position of the maximum density gradient, as shown in Figure 6(b). Edge detection algorithms were subsequently applied to identify the location of the maximum density gradient and the model surface, allowing an estimation of boundary layer thickness. This enabled the estimation of the positions of the maximum density gradient and the model surface is denoted as  $\delta_p$ . Streamwise distributions of the positions of the maximum density gradient were

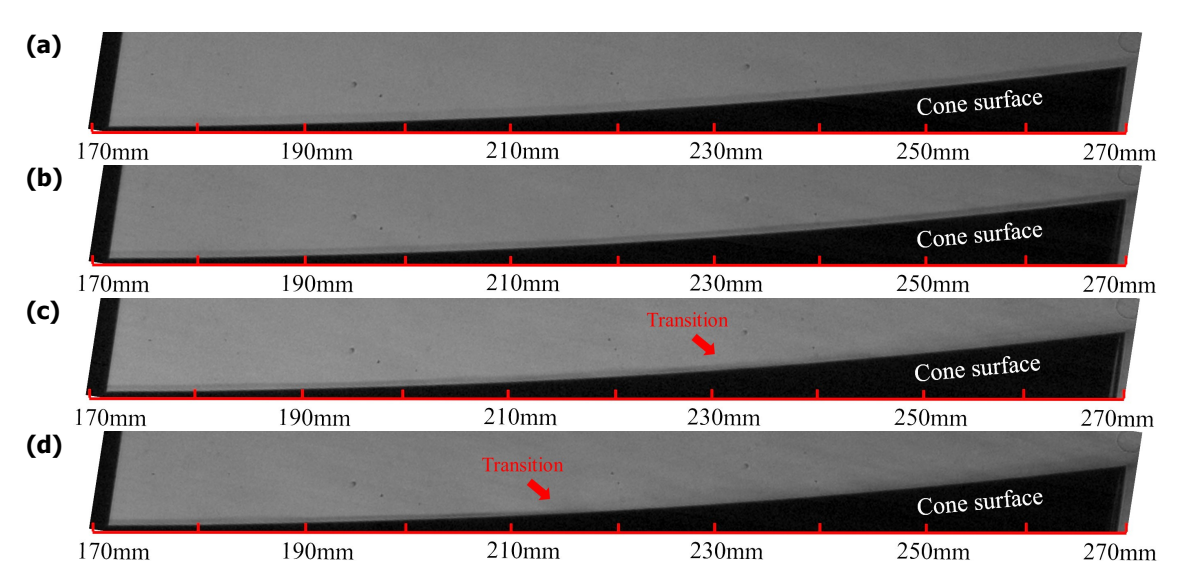
calculated at each time step and time-averaged over 595 images, as shown in Figure 6(d). The schlieren data revealed that transition corresponds to regions exhibiting significant temporal fluctuations in the position of the maximum density gradient. To quantify this behavior, the root mean square (RMS) of  $\delta_p$  was calculated along the streamwise direction, as presented in Figure 6(e). In the present experiments, the coordinate system is defined such that x, y, and z represent the streamwise, spanwise, and wall-normal directions, respectively, in the upstream flow over the flared cone, with x=0 corresponding to the cone tip.

For the smooth-wall baseline case, transition onset is identified at approximately x=215 mm using the RMS method, while the time-averaged method estimates it closer to x=205 mm. Compared to the instantaneous image shown in Figure 6(b), the time-averaged method consistently places the transition point further upstream—by about 15 mm, a trend that also holds true for the riblet cases. More precisely, the time-averaged approach detects the initial region where disturbance amplitudes begin to grow and the boundary layer thickens, whereas the RMS method identifies the point where disturbance amplitudes peak and the boundary layer approaches the end of its transition. In this paper, the streamwise distributions of the time-averaged and RMS value of  $\delta_p$  are present to provide a more complete representation of the effects of riblets on the transition process.

#### 3. Results and discussion

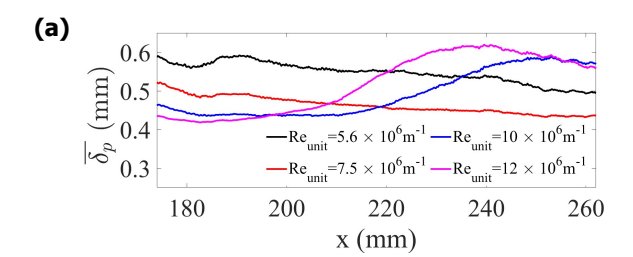
## 3.1. Baseline results at different Reynolds numbers

We first conducted a schlieren experiment on a smooth wall to visually examine the evolution of the conical boundary layer at four different unit Reynolds numbers: Re<sub>unit</sub> =  $5.6 \times 10^6$  m<sup>-1</sup>,  $7.5 \times 10^6$  m<sup>-1</sup>,  $10 \times 10^6$  m<sup>-1</sup>, and  $12 \times 10^6$  m<sup>-1</sup>. The imaging region extended from 170 mm to 270 mm downstream of the model's tip, with the incoming flow direction from left to right.



**Fig 7.** Schlieren images for the smooth wall at different Reynolds numbers: (a)Re<sub>unit</sub> =  $5.6 \times 10^6$  m $^{-1}$ , (b)Re<sub>unit</sub> =  $7.5 \times 10^6$  m $^{-1}$ , (c)Re<sub>unit</sub> =  $10 \times 10^6$  m $^{-1}$  and (d)Re<sub>unit</sub> =  $12 \times 10^6$  m $^{-1}$ .

As shown in Figure 7(a), at  $Re_{unit} = 5.6 \times 10^6 \ m^{-1}$ , the boundary layer is thick and laminar, with no distinct flow structures visible. As the unit Reynolds number increases, as in Figure 7(b), the boundary layer becomes thinner, though the edge of the laminar boundary layer remains visible toward the rear of the model. At  $Re_{unit} = 10 \times 10^6 \ m^{-1}$ , shown in Figure 7(c), the boundary layer begins to transition, and the outer edge of the laminar region disappears around  $x=230 \ mm$ . When the Reynolds number increases further to  $Re_{unit} = 12 \times 10^6 \ m^{-1}$ , as shown in Figure 7(d), the transition occurs earlier, with the disappearance of the laminar boundary layer edge occurring approximately at  $x=210 \ mm$ .



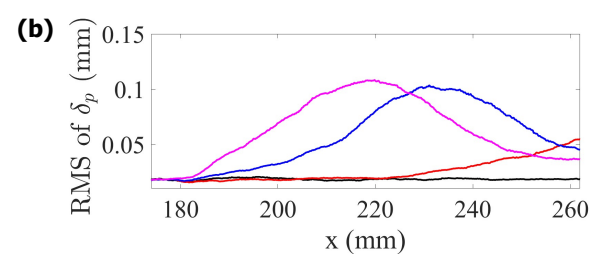


**Fig 8.** (a) Time-averaged value and (b) root-mean-square (RMS) value of  $\delta_p$  for the smooth wall at different Reynolds numbers.

Figure 8(a) shows the streamwise variations of  $\overline{\delta_p}$  for the smooth wall at various Reynolds numbers. Initially,  $\overline{\delta_p}$  decreases with streamwise distance for all cases, indicating boundary layer thinning. At Re<sub>unit</sub> =  $5.6 \times 10^6$  m<sup>-1</sup> and Re<sub>unit</sub> =  $7.6 \times 10^6$  m<sup>-1</sup>,  $\overline{\delta_p}$  continues decreasing until the end of the flared cone, suggesting that the boundary layer remains laminar throughout the entire model length. In contrast, a gradual increase occurs around x=210 mm in  $\overline{\delta_p}$  at Re<sub>unit</sub> =  $10 \times 10^6$  m<sup>-1</sup> implies boundary layer growth and a possible start of transition over the flared cone. At Re<sub>unit</sub> =  $12 \times 10^6$  m<sup>-1</sup>, the increase in  $\overline{\delta_p}$  shifts upstream to approximately to x=190 mm indicating a more rapid development of the boundary layer and an earlier onset of transition.

Additionally, as shown in Figure 8(b), the RMS peak of  $\delta_p$  at Re<sub>unit</sub> =  $5.6 \times 10^6$  m $^{-1}$  remains nearly zero and constant, indicating high stability of the laminar boundary layer. The continuous increase in the RMS peak of  $\delta_p$  at Re<sub>unit</sub> =  $7.5 \times 10^6$  m $^{-1}$  suggests that the boundary layer is developing but remains laminar. At Re<sub>unit</sub> =  $10 \times 10^6$  m $^{-1}$ , the RMS peak of  $\delta_p$  peaks around x=230 mm which corresponds to where rapid fluctuations of the boundary layer thickness occur as observed in the schlieren images (see Figure 7(c)). At Re<sub>unit</sub> =  $12 \times 10^6$  m $^{-1}$ , this location is shifted upstream to around x=220 mm.

#### 3.2. Effects of changing riblet location and height on transition

After the performance of the baseline cases is established, riblets were applied to the surface of the flared cone. Experiments were carried out at a Reynolds number of  $\text{Re}_{\text{unit}} = 10 \times 10^6 \text{ m}^{-1}$  to evaluate the effects of changing riblet location and riblet height.

# 3.2.1. Riblet location

Yaw angle	Spacing	Width	Spanwise wavelength	Gap size	Total length
$\alpha = 30^{\circ}$	s = 4h	$\Lambda=6 \mathrm{mm}$	w= <b>5.2mm</b>	$\Lambda-w$ =0.8mm	l=20mm

**Table 1.** Key geometric parameters of the riblets.

An array of five herringbone riblet sections with h=54  $\mu$ m adhered on a 45  $\mu$ m thick substrate ( a total height  $H\approx 100\mu$ m) were installed at two streamwise locations along the model: x=170 mm and x=230 mm. The first location corresponds to where disturbances grow rapidly and where transition may initiate, while the second location corresponds to a region where the flow is nearly turbulent. Riblets installed at these two specific locations may exhibit great potential to delay the transition process. The yaw angle was fixed at 30°, the riblet spacing was set to s=4h, and the spanwise wavelength was fixed at 6 mm. The total length of the riblet section was maintained at 20 mm. Detailed riblet parameters are provided in Table 1.

Schlieren images reveal that the boundary layer over the smooth wall becomes unstable around x=220 mm, as shown in Figure 9(a). In Figure 9(b), the schlieren images indicate that riblets placed at x=170 mm generate weak compression waves, and the onset of long-wave disturbances occurs at approximately the same location as on the smooth wall. In contrast, riblets positioned at x=230

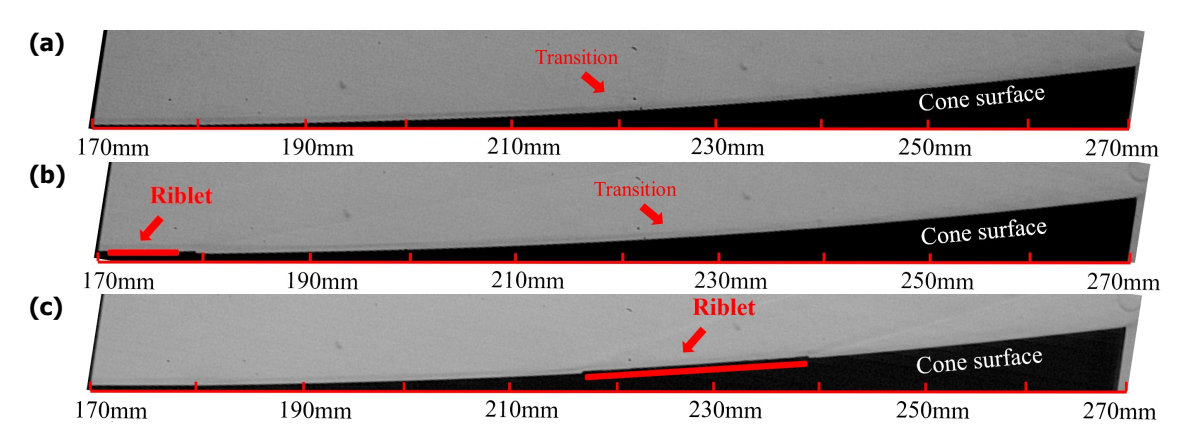


**Fig 9.** Schlieren images for (a) smooth wall and riblets placed at (b) x=170 mm and (c) x=230 mm.

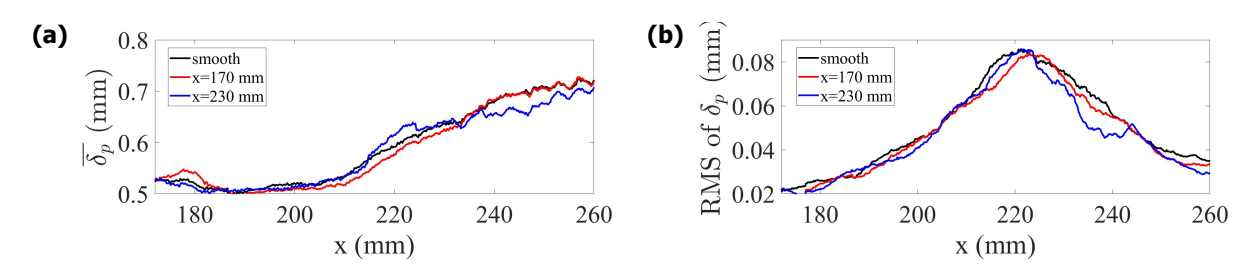


**Fig 10.** (a) Time-averaged value and (b) root-mean-square (RMS) value of the position of the maximum density gradient,  $\delta_{\nu}$ , for both the smooth wall and riblets with h=54  $\mu$ m.

mm produce stronger compression waves and induce more significant disturbances within the boundary layer, as illustrated in Figure 9(c).

To quantify the transition behavior of the boundary layer from the schlieren images, the time-averaged and root mean square (RMS) values of the maximum density gradient position,  $\delta_p$ , were computed along the streamwise direction. As shown in Figure 10(a), the time-averaged  $\delta_p$  for both the smooth wall and the case with riblets of height  $h=54~\mu{\rm m}$  placed at  $x=230~{\rm mm}$  begins to increase around  $x=200~{\rm mm}$ . In contrast, for the configuration with riblets placed at  $x=170~{\rm mm}$ ,  $\delta_p$  starts to rise approximately at  $x=210~{\rm mm}$ . These results indicate that riblets with a height of  $h=54~\mu{\rm m}$  slightly delay the onset of transition when positioned at  $x=170~{\rm mm}$ . Additionally, the RMS peak of  $\delta_p$  for the riblets placed at  $x=170~{\rm mm}$  appears approximately 10 mm downstream of the peaks observed in the other cases, as shown in Figure 10(b), and this finding is consistent with the finding from the distribution of  $\delta_p$ .

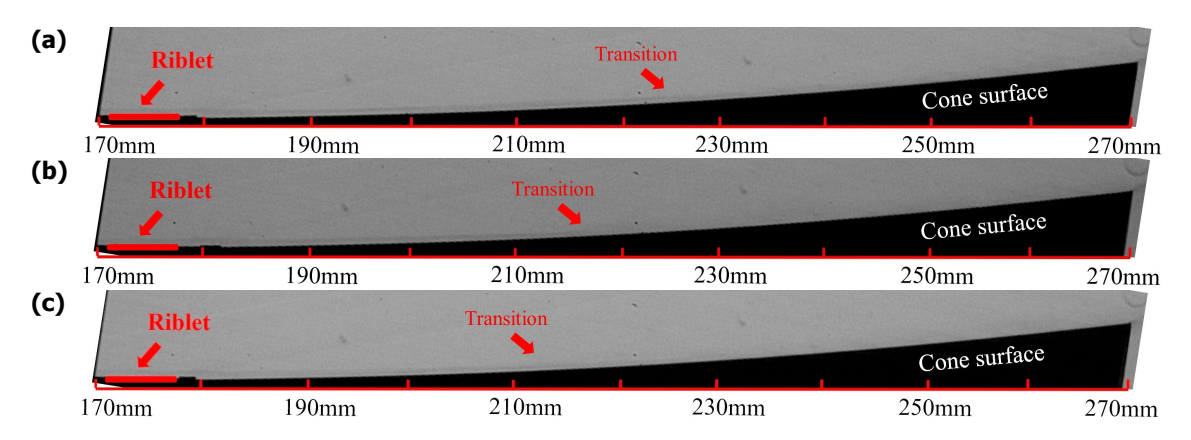
## 3.2.2. Riblet height



Fig 11. Layout of herringbone riblets with different heights: (a)  $h=54\mu\text{m}$ , (b)  $h=140\mu\text{m}$  and (c)  $h=215\mu\text{m}$ .

Based on the previous investigation, riblets with three different heights, h = 54  $\mu$ m, 140  $\mu$ m, and

215  $\mu$ m, were installed at x=170mm to examine the effects of riblet height on the onset of transition. The layout of herringbone riblets is shown in Figure 11. Each riblet array was adhered to a 45 $\mu$ m-thick substrate. The yaw angle was fixed at  $30^{\circ}$ , the riblet spacing was set to s=4h, and the spanwise wavelength was maintained at 6mm. The total length of the riblet section was kept at 20mm.



**Fig 12.** Schlieren images of riblets placed at the streamwise position x=170 mm: (a)  $h=54\mu\text{m}$ , (b)  $h=140\mu\text{m}$  and (c)  $h=215\mu\text{m}$ .

As shown in Figure 12, downstream of the riblets, around x=180 mm, the boundary layer is lifted due to the presence of the riblets, with this effect becoming more significant as riblet height increases. Moreover, the identifiable extent of the boundary layer edge decreases for taller riblets. These results reveal a clear trend: increasing riblet height leads to stronger boundary layer disturbances and possibly an earlier transition.

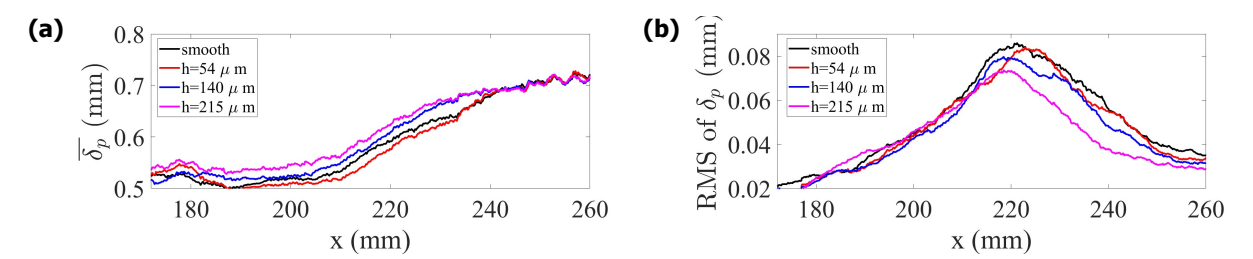


**Fig 13.** (a) Time-averaged value and (b) root-mean-square (RMS) value of  $\delta_p$  for riblets placed at x=170 mm.

The quantitative analysis presented in Figure 13 clearly demonstrates that riblets placed at x=170mm with a height of  $54\mu\text{m}$  can delay the transition, whereas riblets with heights of  $140~\mu\text{m}$  and  $215~\mu\text{m}$  tend to promote it. The riblet with  $h=54~\mu\text{m}$  leads to a delayed rise in  $\overline{\delta_p}$ , compared to the smooth wall case. In contrast, the riblets with  $h=140~\mu\text{m}$  and  $h=215~\mu\text{m}$  result in a thicker  $\overline{\delta_p}$  and earlier rise in  $\overline{\delta_p}$ , suggesting a more rapid boundary layer development, as shown in Figure 13(a). Furthermore, the peak location of the RMS of  $\delta_p$  for the riblet with  $h=54~\mu\text{m}$  is approximately 10mm downstream of that for the smooth wall, indicating that the onset of turbulence occurs further downstream with this riblet configuration. Conversely, the peak location for the riblets with  $h=140\mu\text{m}$  and  $h=215\mu\text{m}$  appear about 10mm upstream of that in the baseline case indicating an earlier transition. The detailed physical mechanism by which riblets delay the transition requires further investigation using PCB pressure sensors in subsequent experiments.

#### 4. Conclusion

A systematic experimental campaign was conducted in the Manchester High-Supersonic Wind Tunnel (HSST) at Ma=5 to investigate the effects of herringbone riblets on the onset of boundary layer transition

in hypersonic flow over a flared cone. In this investigation, schlieren was employed to obtain both qualitative and quantitative data to gain an insight of such impact produced by riblets placed at two different streamwise locations along the model and riblets with different heights.

It was found that while riblets with a height of 54  $\mu$ m produced a negligible effect on transition when they were placed at x=230 mm at Re<sub>unit</sub> =  $10\times10^6$  m<sup>-1</sup>, they result in a delayed transition when they are placed x=170 mm. Furthermore, taller riblets placed at x=170 mm were found to promote earlier transition as evident by an upstream shift of the locations where the time-averaged boundary layer thickness begins to increase and the peak RMS value of boundary layer thickness occur. Our study demonstrates the potential of herringbone riblets as a means of effective flow control in hypersonic flow.

#### References

- [1] Morkovin, M.V, Transition in open flow systems a reassessment. Bull. Am. Phys. Soc. 39, 1882 (1994).
- [2] Fedorov, A. Transition and stability of high-speed boundary layers. Annu. Rev. Fluid Mech. 43, 79–95 (2011).
- [3] Zhong, X. and Wang, X. Direct numerical simulation on the receptivity, instability, and transition of hypersonic boundary layers. Annu. Rev. Fluid Mech. 44, 527–561 (2012).
- [4] Lee, C. and Chen, S. Recent progress in the study of transition in the hypersonic boundary layer. Natl Sci. Rev. 6, 155–170 (2018).
- [5] Fong K, Wang X, Huang Y, Zhong X and McKiernan RG, Fisher RA and Scheider SP, Second Mode Suppression in Hypersonic Boundary Layer by Roughness: Design and Experiments, AIAA Journal, 53(10), 3138-3144 (2015).
- [6] Fujii K, Experiment of the two-dimensional roughness effect of hypersonic boundary-layer transition, J. Spacecraft Rockets, 43(4), 731-738 (2006).
- [7] Holloway, P., and Sterrett, J., Effect of Controlled Surface Roughness on Boundary-Layer Transition and Heat Transfer at Mach Number of 4.8 and 6.0, NASA TR-D-2054 (1964).
- [8] Paredes P, Choudhari MM and Li F, Transition delay via vortex generators in a hypersonic boundary layer at flight conditions, AIAA 2018-3217 (2018).
- [9] Fedorov, A.V., Shiplyuk, A., Maslov, A., Burov, E., Malmuth, N.: Stabilization of a hypersonic boundary layer using an ultrasonically absorptive coating. J. Fluid Mech. 479, 99–124 (2003).
- [10] Wartemann, V., Wagner, A., Surujhlal, D., and Dittert, C. OCTRA as ultrasonically absorptive thermal protection material for hypersonic transition suppression. CEAS Space Journal, 15(6), 959-969 (2023).
- [11] Chen, H., Rao, F., Shang, X., Zhang, D., and Hagiwara, I., Flow over Bio-Inspired 3D Herringbone Wall Riblets, Exp Fluids 55, 3, 1–7 (2014).
- [12] Xu, F., Zhong, S., and Zhang, S., Vortical Structures and Development of Laminar Flow Over Convergent-Divergent Riblets, Phys. Fluids, 30(5), 051901 (2018).
- [13] Kevin, K., Monty, J. P., Bai, H. L., Pathikonda, G., Nugroho, B., Barros, J. M., Christensen, K. T., and Hutchins, N., Cross-Stream Stereoscopic Particle Image Velocimetry of a Modified Turbulent Boundary Layer Over Directional Surface Pattern, J. Fluid Mech., 813, 412–435 (2017).
- [14] Xu, F., Zhong, S., and Zhang, S., Statistical Analysis of Vortical Structures in Turbulent Boundary Layer Over Directional Grooved Surface Pattern With Spanwise Heterogeneity, Phys. Fluids, 31(8), 085110 (2019).

- [15] Liu, Q., Zhong, S. and Li, L., Investigation of riblet geometry and start locations of herringbone riblets on pressure losses in a linear cascade at low Reynolds numbers. Journal of Turbomachinery, 142(10), 101010 (2020).
- [16] Quan, P., Zhong, S., Liu, Q. and Li, L., Attenuation of flow separation using herringbone riblets at  $M_{\infty}$  = 5. AIAA Journal, 57(1), 142-152 (2019).
- [17] Wen, B., Zhong, S., Wang, G., and Li, L. Effects of herringbone riblets on shock-wave/turbulent boundary-layer interactions. AEROSP SCI TECHNOL, 146, 108914 (2024).
- [18] Zhu, W. K. and Shi, M.T. and Zhu, Y. D. and Lee, C. B., Experimental study of hypersonic boundary layer transition on a permeable wall of a flared cone, Phys. Fluids 32, 011701 (2020).
- [19] Zhu, W. K. and Gu, D. W. and Si, W. F. and Zhang, M. J. and Chen, S. Y. and Smith, C. R. and Zhu, Y. D. and Lee, C. B., Instability evolution in the hypersonic boundary layer over a wavy wall, J. Fluid Mech. 943, A16 (2022).
- [20] Erdem, E and Kontis, K and Johnstone, E and Murray, NP and Steelant, Johan, Experiments on transitional shock wave--boundary layer interactions at Mach 5, Exp Fluids 54, 1598 (2013).